HIGH-RESOLUTION SPECTROSCOPIC STUDIES OF CARBON-CONTAINING SPECIES

BY

NICOLE C. KOEPPEN

THESIS

Submitted in partial fulfillment of the requirements
for the degree of Master of Science in Chemistry
in the Graduate College of the
University of Illinois at Urbana-Champaign, 2016

Urbana, Illinois

Adviser:

Professor Benjamin J. McCall

Abstract

High-resolution spectra of molecules and ions can provide valuable information fundamentally and astrochemically. From the fundamental side, high-resolution rovibrational spectroscopy allows molecular constants to be determined and provides evidence of theoretical assumptions. Work to this end was performed using cavity-ringdown spectroscopy and either a gas phase or supercritical fluid supersonic expansion source. Future work will focus on optimizing the supercritical fluid source, in addition to setting up a positive column for the study of molecular ions. Astrochemically, rovibrational and rovibronic spectroscopy can allow for the column density of species to be determined towards different sightlines in the interstellar medium. This is accomplished by either obtaining laboratory absorption spectra of species of interest to compare to astronomical observations or by using fitting procedures and modeling programs to analyze previously obtained astronomical spectra. Laboratory spectra from gas phase and supercritical phase 1,3,5-trioxane, and fitting and modeling procedures for the analysis of C_3 are included. In addition, future goals for each project, including a proposed ion source for cavity ringdown spectroscopy, are described.

To my friends and family, for all their support.

Acknowledgments

First, I would like to thank my advisor, Ben McCall, for his support and guidance throughout my time on these projects. Also, I want to acknowledge Brad Gibson for the valuable information and spectroscopic techniques I learned from him, in addition to what I learned from working on the trioxane spectrum together. I also want to thank Peter Kiamanesch and Amber Rose for their help in building and maintaining various aspects of the laser system.

I would also like to thank the rest of the McCall Group for their conversations and feedback whenever I had questions or just needed an extra hand with the experiment: Courtney Talicska, Scott Dubowsky, Charlie Markus, Adam Perry, James Hodges, and Mike Porambo. Outside of the McCall group I would like to thank Kyle Webb, who was always willing to help us maintain and fix our vacuum pump when it happened to break down.

Lastly, I would especially like to thank Tyler Naibert for all his support and technical insight, in addition to his willingness to provide me with excessive amounts of coffee and fun distractions from lab.

Table of Contents

Chapter 1

Advantages of High-Resolution Infrared Spectroscopy

High-resolution spectroscopy in the infrared (IR) region of the electromagnetic spectrum has many advantages. Fundamentally, high-resolution IR spectroscopy has the ability to probe the combined rotational-vibrational (rovibrational) transitions of a molecule. This is especially useful when the molecule of interest does not have a permanent dipole moment, making purely rotational transitions forbidden. In these cases, rotational data can be obtained through the use of rovibrational transitions. Since these transitions combine both a change in rotational state and a change in vibrational state, the intensity of the transitions, S, only require that the dipole of the molecule, μ, change with respect to the radius, r, following the proportionality given below [1].

$$S_{J'J''} \propto \left| \frac{d\mu}{dr} \right|_{r_e}^2 \tag{1.1}$$

This allows for the extraction of rotational energy levels and constants to be indirectly determined for molecules without a permanent dipole moment.

Observationally, the far mid-IR around 1180 cm^{-1} has an advantage of being visible through our atmosphere. The atmosphere on Earth has a significant contribution from carbon dioxide and water, both of which absorb in the IR region of the spectrum. The main absorption regions for these species largely occur at wavelengths less than 8 μm, making it impossible to observe transitions through the atmosphere in these regions. Near the 8.5 μm wavelength region there are no major atmospheric species which absorb, which creates a window for ground-based telescopes to observe regions beyond our atmosphere at these wavelengths.

Chapter 2

Experimental

2.1 Overview of Experimental Layout

The system used in this work for high-resolution mid-IR cavity ringdown spectroscopy (CRDS) includes a continuous-wave external-cavity quantum cascade laser (cw-EC-QCL) centered around 8.5 μm [2]. The beam from this source is split with a 50/50 beam-splitter, with one arm directed towards a side-of-fringe (SOF) locking system, and the other arm through a germanium acousto-optic modulator (AOM)(ISOMET 1207B). The AOM is used to diffract the light to different optical elements and also to provide a fast-shuttering system for CRDS. While the AOM is switched off, the entirety of the zeroth order light is directed towards a Bristol 621B wavemeter for relative frequency calibration. When the AOM is switched on, the majority of the light is diffracted to the first order and sent towards a polarizer and Fresnel rhomb for backscatter isolation of the laser, and then some of the light is split towards a reference cell using a beam-splitter. The reference used for the absolute frequency calibration is SO_2, whose transitions in this region are well-known and available from the HITRAN database [3]. The rest of the light is sent through a hollow silica waveguide (HSW)(Opto-Knowledge) and into the vacuum chamber where the sample is introduced and the cavity is created. The transmitted light from the cavity is then collected using a photovoltaic mercury-cadmium-telluride (PV-MCT)(Kolmar Technologies) detector.

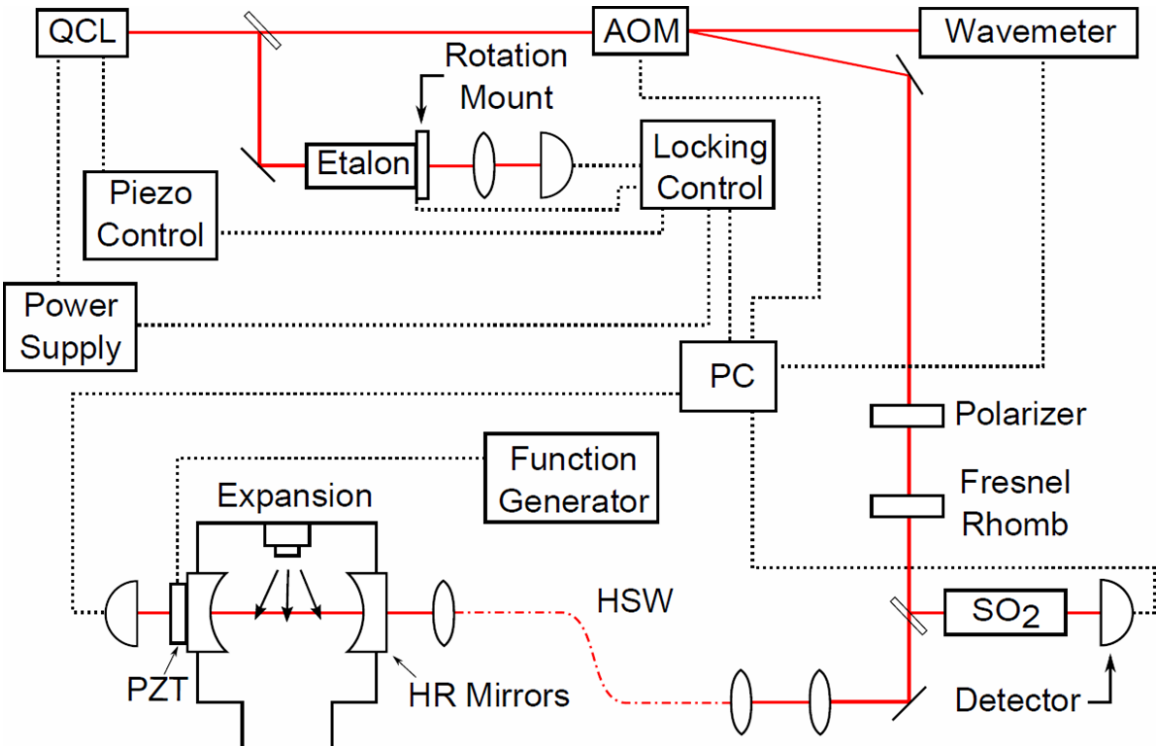

Figure 2.1: cw-EC-QCL CRDS experimental setup. Shown is a block diagram of the experimental setup used for CRDS. The laser light from the EC-QCL is split, with half going towards the SOF locking system and the other half used for data acquisition. When the AOM is off, the light is directed towards the wavemeter for calibration and when it is switched on the light is directed towards the cavity and SO_2 cell. Once the light reaches the cavity, it is coupled in using a HSW. The cavity length is dithered with the PZT and the resulting ringdown data is then collected and processed. Figure adapted from [4].

2.1.1 External-Cavity Quantum Cascade Laser

The EC-QCL has a scanning range of 1135 cm^{-1} to 1220 cm^{-1}, with mode-hop free scanning of around 0.4 cm^{-1} [2]. The laser consists of a QCL chip, which is housed in a laser mount and placed under vacuum to discourage condensation which could damage the laser. The chip is kept in thermal contact with a copper block and connected to a thermoelectric cooler (TEC), which maintains a low and constant temperature to the nearest 0.001^oC. Additionally the laser is water cooled, which assists in removing excess heat from the system and allows the TEC to maintain lower temperatures. To scan through different frequencies three elements are simultaneously adjusted; the injection current to the QCL chip, the external cavity length, and the angle of the diffraction grating. The diffraction grating is positioned such that the reflection from the first order light is directed back into the laser and produces the cavity. The zeroth order light is reflected

to an output mirror and used for spectroscopy. A picture of the laser system can be seen in Figure 2.2. Because of the external component to the laser, there initially existed an inherent frequency jitter of ∼130 MHz over a 1 second integration time. In order to perform high-resolution work with the laser, a locking mechanism was implemented to reduce the jitter.

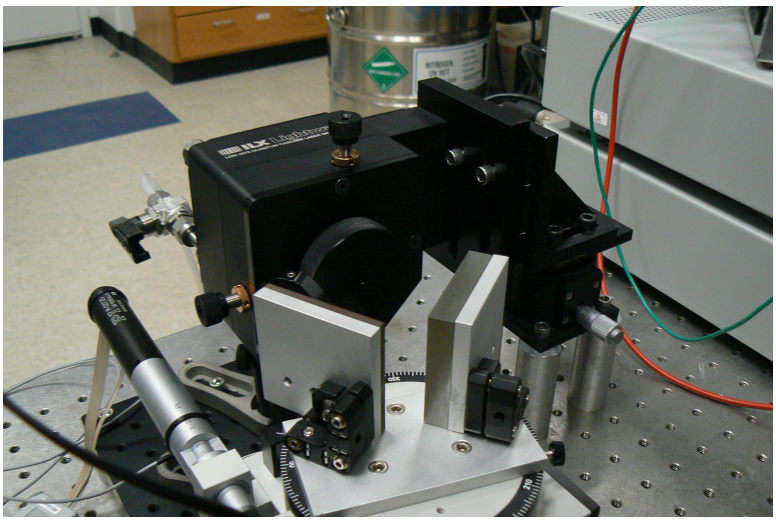

Figure 2.2: EC-QCL. The enclosed portion of the EC-QCL contains the QCL chip, which is centered ∼8.5 μm. The external grating produces the cavity and allows for a reasonably broad range of frequency values for the laser.

2.1.2 Side-of-Fringe Locking System

The frequency jitter of the laser was reduced using a novel SOF locking system. The detailed setup and operation of the system are described in detail in Gibson *et. al* [5]. Briefly, a 2" solid germanium etalon (Light Machinery) is introduced into the laser path and mounted on an Agilis AG-M100L piezo-driven optic mount (Newport). Since the free spectral range (FSR) of an etalon is inversely related to the cosine of the angle of light propagation within the etalon relative to its surface, tilting the etalon in relation to the incident light changes the FSR. This in turn proportionally affects the fringes produced by the etalon. Using this concept, an analog locking circuit was made which tilts the etalon in steps such that the laser frequency remains locked onto the side of one of the fringes as it is scanned. The feedback from the lock moving up or down the fringe is used to control all three adjusting elements of the laser. Additionally, due to the index of refraction for germanium being extremely temperature dependent, an enclosure was built around the etalon to minimize inaccuracies due to temperature variations. With this system in place, the frequency jitter was reduced to ∼1 MHz over a 1 second integration time, enabling a mode-hop free scanning range of ∼0.4 cm^{-1}

with steps of ∼12 MHz.

2.1.3 Backreflection Isolation System

Because of the properties of the EC-QCL, backreflections into the cavity are detrimental to the frequency stability of the laser. To prevent this, a backscatter isolation system was put into place using both a wire-grid polarizer and a Frensel rhomb as described in [6]. Because of the orientation of the QCL chip and laser mounting, the light output from the EC-QCL is horizontally polarized. After passing through the AOM, the light is directed through the wire-grid linear polarizer and is then circularly polarized when it passes through the Fresnel rhomb. Any backreflections become circularly polarized in the opposite direction, pass back through the Fresnel rhomb, become vertically polarized, and are then blocked by the polarizer.

2.1.4 Cavity Ringdown

CRDS relies on a pair of highly reflective mirrors (R = 0.9995, Laser Power Optics) which form a cavity and significantly increase the pathlength of the light. A piezoelectric transducer (PZT)(Piezomechanik) is used to dither one of the mirrors and modulate the cavity length by greater than one free spectral range (FSR) at a rate of ∼60 Hz. This enables the cavity to be on-resonance with the laser twice per cycle and the light inside the cavity to build up to a user-defined threshold. Once it reaches this point, the AOM switches off and the light intensity is allowed to ringdown. The time it takes for this to occur is based on the reflectivity of the mirrors, the length of the cavity, and any absorbing species within the path of the light. The time constant, τ, is defined by the amount of time it takes the light to decay to ⅟ₑ of its original power. Using this time constant, the absorption at that wavelength is then determined by fitting the resulting exponential function to the standard CRD equation which relates the intensity, $I(t)$, to the initial intensity, I_o [7].

$$I(t) = I_o exp\left(\frac{-t}{\tau}\right) \tag{2.1}$$

This highlights a major advantage of CRDS in that the data is independent of any laser fluctuations that may occur between readings since the time constant is based only on the decay of the light. For the purposes of this specific work, 100 ringdowns were collected for each wavelength, and the middle 50 points were selected using a box-and-whiskers algorithm and averaged to give the time constant for that point.

2.2 Supercritical Fluid Source Expansion

Another novel aspect of this system is the method with which samples are introduced. Although other gas phase expansions have also been studied with this system [4], the ultimate goal is to create a reliable supercritical fluid (SCF) expansion, which can be used to observe molecules which do not have a low enough vapor pressure for gas phase spectroscopy to be effective.

The experimental design of the source was built with a number of necessary parameters in mind. The first being that the system would have to reach and withstand high temperatures and pressures. In addition, the sample reservoir would have to be placed outside the main vacuum chamber to allow for refilling without needing to bring the entire system back up to atmospheric pressure. To accomplish these, liquid CO_2 and toluene, saturated with the molecule of interest, are combined in a high-pressure syringe pump (ISCO μL-500). This pump then pushes the mixture into the source chamber, fabricated from a 2" x 2" x 5" block of stainless steel with a 1" diameter hole through the center. All fittings were either high-pressure NPT or taper-seal fittings rated up to 15,000 psi (High Pressure Equipment Company) and were attached with Loctite 567 high-temperature thread sealant. On one end of the steel block, a high-pressure sight-window rated up to 4,000 psi (Rayotek) is placed such that any phase separation can be seen. On the outside of the source, two heating plates are attached which allow the source to reach temperatures of $\sim$450 K, monitored by a thermocouple in the solution. Once the mixture reaches the temperature and pressure needed for SCF to form, a two-way valve (High Pressure Equipment Company) is opened, which allows the SCF to come up through a 10 μm pinhole (Lenox Laser), become entrained in argon gas, and then expanded through a 12.7 mm x 150 μm slit nozzle. The nozzle apparatus is thermally connected to the main source chamber in order to maintain the SCF until it is expanded into the chamber. This setup is based off designs by Goates *et al.* [8]

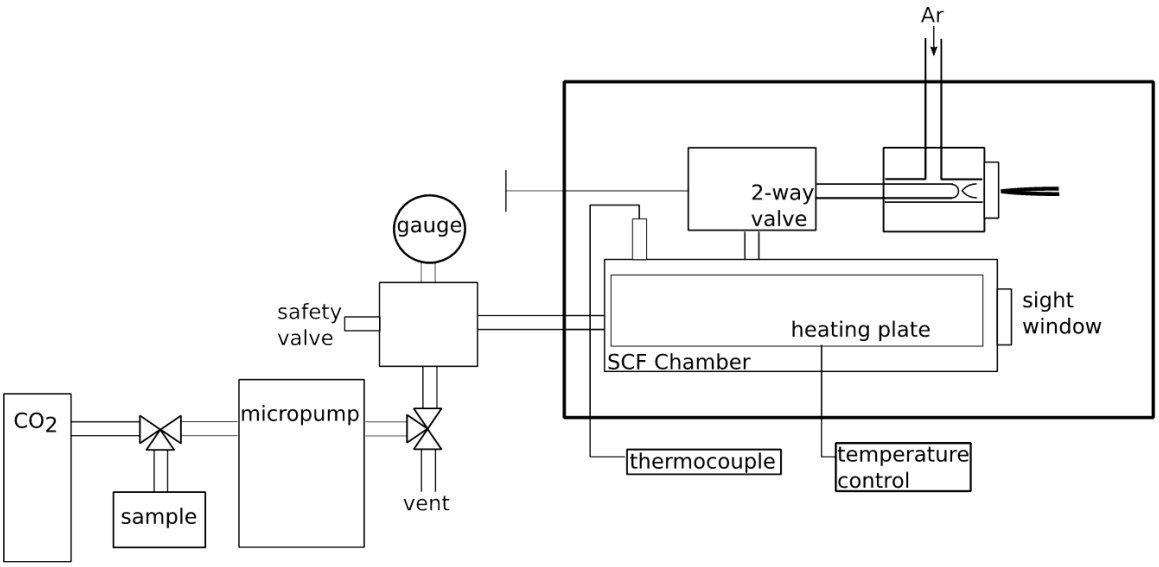

Figure 2.3: SCF experimental setup. Shown is a block diagram of the system used for the introduction of SCF into the chamber. CO_2 and a toluene/solute solution are combined in the micropump. The total solution is then pumped into the SCF source chamber where heating plates heat the solution. Once SCF temperature and pressure are reached, the solution is allowed to expand through a pinhole and become entrained in Ar carrier gas. This is then supersonically expanded through the slit and into the chamber.

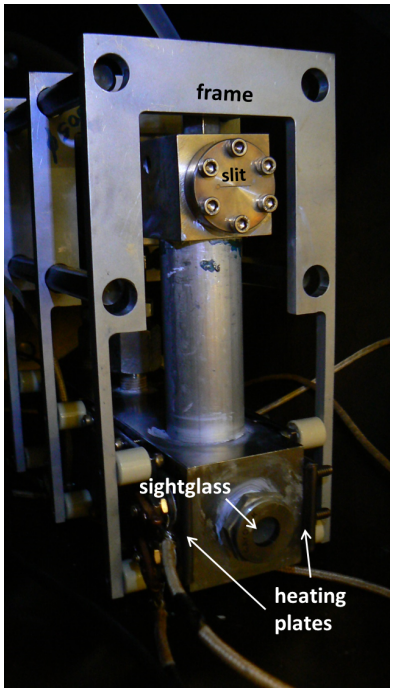

Figure 2.4: SCF source chamber. The SCF source chamber with the sightglass, heating plates, and slit expansion shown. The system is attached to a frame for precise placement inside the vacuum chamber.

Chapter 3

Trioxane Spectroscopy

Before attempting to obtain a spectrum of C_{60} we wanted to obtain a spectrum of a highly absorbing molecule which we could use to optimize our system. We found that 1,3,5-trioxane has a strongly absorbing ν_{16} band centered around 1177 cm^{-1}, which is within the range of our laser system. In addition, trioxane also has astronomical significance in cometary studies.

3.1 Astronomical Background

Trioxane is part of a class of molecules called polyoxymethylenes (POMs). These molecules are thought to be a possible source of formaldehyde, which has been previously detected in cometary comae [9, 10]. This possible correlation makes trioxane an important molecule when it comes to prebiotic studies. Although no direct cometary trioxane observations have been made to this date, laboratory simulations of cometary comae have been completed and trioxane was detected as a product from the photodegredation of larger POMs [9]. Trioxane is also a relatively volatile POM, which makes it a good candidate as a formaldehyde or POM tracer in the future.

3.2 Spectroscopic Background

Trioxane is a symmetric top of the C_{3v} point group. The ground state microwave spectrum was first observed in 1963 by Oka *et al.* [11], and additional rotational spectra of some of the excited states have been obtained since then [12–16]. The rovibrational band of ν_{17} was observed in 1992 by Henninot *et al.* [17], which was the only rotationally-resolved vibrational data available until 2015 [4].

3.3 Gas Phase Spectrum and Assignment

In order to use trioxane to optimize the system for SCF expansion we began by collecting a gas phase spectrum. Argon was used as the carrier gas for a slit supersonic expansion at 2 atm backing pressure. The argon flow was split into two paths before the sample introduction, with one being sent through solid trioxane. A needle valve present directly after the trioxane allowed the amount of trioxane within the argon flow to be adjusted since both flow paths were recombined before the supersonic expansion. In addition, tubes were placed between the mirrors and expansion and a steady flow of nitrogen gas was maintained in order to limit the amount of room-temperature trioxane contaminating the mirrors in the chamber.

A majority of the spectrum of the ν_{16} band was obtained between 1175.93 - 1179.28 cm^{-1}, which included many Q-branch transitions as well as some of the transitions from the P and R branches. Fitting of the spectrum was performed using a program called PGOPHER [18]. Overall, 219 transitions were fit with an average residual of 26.02 MHz and excited state spectroscopic constants were obtained. The ground state parameters were set to values from Gadhi *et al.* [16], although it is important to note that C" has not yet been experimentally determined and was set at an estimated value of 2950 MHz. Since the origin, Coriolis constant, and C' are dependent on the value of C" these are instead listed in expressions independent of C". The excited state values for the D_J and the sextic centrifugal distortion constants were held at the ground state values.

Between the fitting errors and uncertainties in the wavememter calibration, we have estimated an overall uncertainty in the frequency calibration to be $\sim$32.7 MHz. This limit comes in part from being restricted to taking a wavemeter reading only every 100 points, since the ringdown must be paused in order to divert enough laser power for an accurate reading. We also noticed that the relative intensities of the experimental and simulated spectra sometimes were inconsistent and found that it is an artifact of undersampling the absorption peaks. Scans with smaller step sizes matched the intensities from the simulation well but the signal from the germanium etalon used for frequency locking is temperature dependent and slowly drifts over time. Because of this, the longer time needed for these scans increased the uncertainty of the frequency calibration.

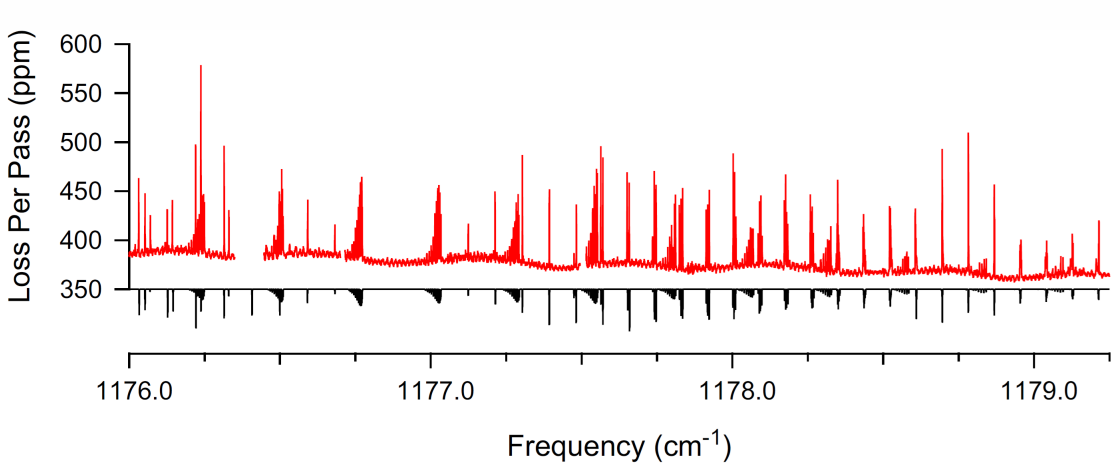

Figure 3.1: Trioxane gas phase spectrum. The trioxane spectrum obtained is shown in the top trace (red). The inverted PGOPHER [18] simulation is shown in the bottom trace (black). Overall 219 lines were observed and assigned.

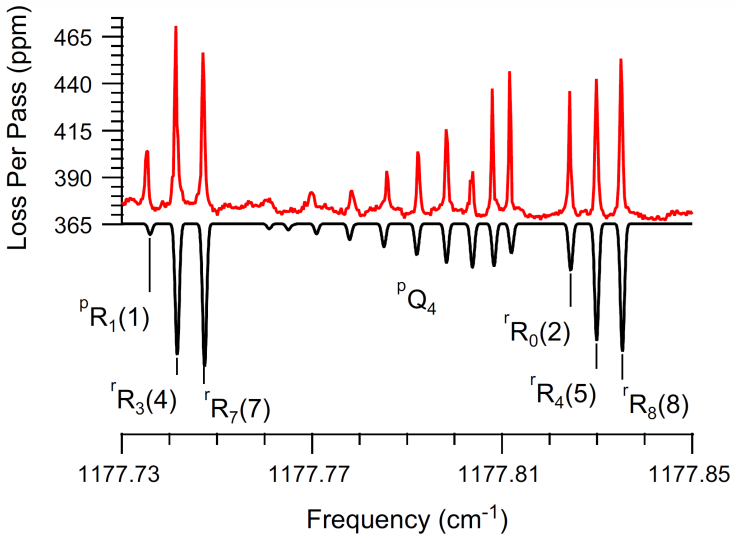

Figure 3.2: Trioxane gas phase spectrum comparison. An expanded view of the trioxane spectrum (top trace, red) between 1177.73 - 1177.85 cm^{-1} and the simulated spectrum (bottom trace, black).

Table 3.1: Trioxane ν_{16} constants. The molecular constants for trioxane were calculated and compared to previous values for the ground state (v = 0) which were obtained from microwave studies [16, 17].

	$v_{16} = 1$	v = 0 [8,16]
$\nu_0 + (C'-B'-2C'\zeta)$ (cm^{-1})	1176.77314(11)	–
B (MHz)	5262.624(51)	5273.25767(20)
$C''-C'$ (MHz)	5.93(12)	–
D_J (kHz)	1.34622	1.34622(34)
D_{JK} (kHz)	−1.97(80)	−2.0243(15)
H_J (Hz)	0.00118	0.00118(10)
H_{JK} (Hz)	−0.00430	−0.00430(40)
H_{KJ} (Hz)	0.0031	0.0031(10)
$C'-B'-C'\zeta$	−3905.81(53)	–
η_J (kHz)	66(11)	–
q^+ (MHz)	2.40(20)	–

3.4 SCF Spectrum

In order to have a majority of molecules present in the ground state, the temperature of the expansion should be as low as possible. To this end, when designing a SCF expansion system, the solvent used should have a relatively low critical temperature. In addition, the solute must be soluble in the solvent chosen. Supercritical CO_2 has a critical temperature of only 304 K, however adding toluene improves the solubility for neutral molecules such as C_{60} [19,20], which is a future molecule of interest. For a 7:3 mole fraction ratio of CO_2:toluene the critical conditions are 1800 psi and 445 K, which is lower than the critical temperature of 592 K for pure toluene [19].

3.4.1 Initial Results

The initial ratio used for the SCF was a 70:30 v/v mixture of CO_2:toluene. This is slightly below the 7:3 mole fraction (50:50 v/v) used in extraction studies [19, 20], but allows the SCF to be formed at lower temperatures. A spectrum of two lines from trioxane were obtained with an SCF expansion of this mixture, with the SCF pressure and temperature ∼3200 psi and ∼433 K. The SO_2 reference cell was not aligned during this scan, which results in the peaks being offset based on the wavemeter readings of the diffracted beam from the AOM. The signal-to-noise ratio (SNR) of the scan was ∼10, which needs to be improved prior to examining other molecules such as C_{60}. One major complication of the current setup is that the thread sealant starts to leak after 2-3 runs with the SCF present and must be re-sealed, making it difficult to continuously run scans.

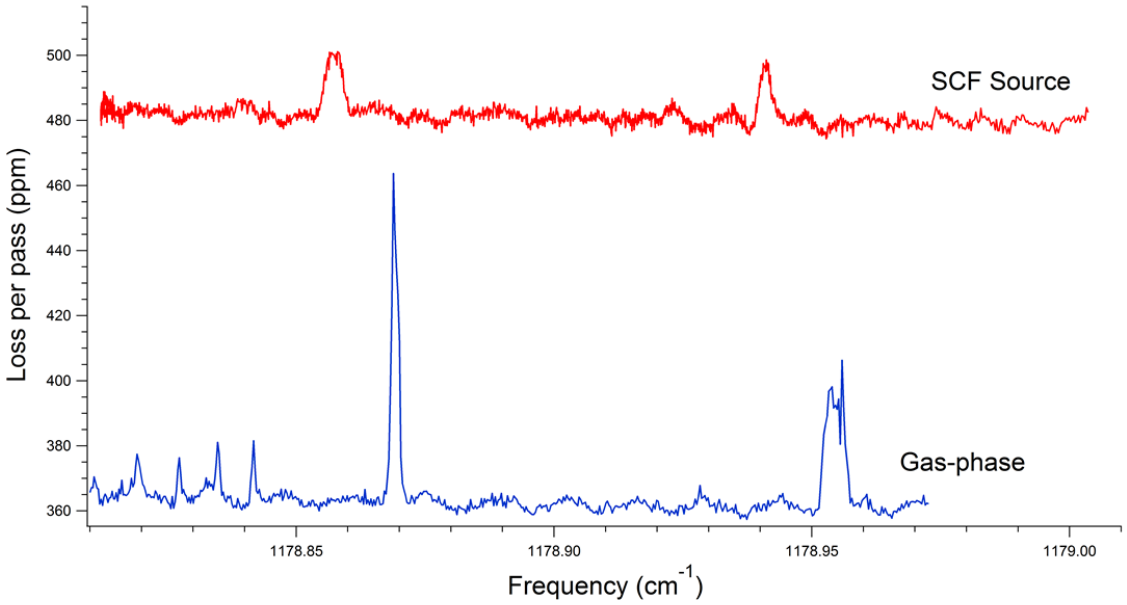

Figure 3.3: SCF trioxane spectrum comparison. The first-attempt at a SCF trioxane spectrum is shown in the top, red trace. The lines are compared to what was previously obtained with gas phase trioxane on the same system. The spectrum is offset because the frequency of the SCF expansion run was only calibrated with wavemeter readings of the zeroth order light.

3.4.2 Future Improvements

Conditions that could be varied in order to improve the SNR would be the ratio of CO_2:toluene and the argon backing pressure. Since toluene is the primary solvent in the solution, using more will allow for a greater mass flow of the molecule of interest in the expansion. However, as toluene has a higher critical temperature, greater ratios of toluene could lead to higher molecular temperatures in the expansion.

It is also possible that deficiencies in the experimental setup are contributing to the poor SNR and broad linewidth. One factor could be insufficient heat at the nozzle. In a similar system, it was found that the minimum nozzle temperature for a CO_2 SCF expansion to work is 393 K [8]. This occurs from an "aerosol-limiting temperature" for the SCF solvent as discovered by Goates *et al.* [21]. The nozzle for our system is heated from thermal transfer through an aluminum block from the SCF source itself making it is possible that the heat is not being transferred efficiently, causing the nozzle to be below the temperature needed for proper aerosol formation. This could also result in the SCF solute being deposited inside the nozzle possibly resulting in clogging and broad lines. Another possible reason for the lack of signal is a velocity mismatch between the SCF expansion and the argon carrier gas. If the velocity of the carrier gas is too low, the SCF

might not be cooled or re-directed through the slit nozzle effectively through collisions. On the other hand, too high of a carrier gas backing pressure might cause turbulent flow which would disrupt the expansion [21]. These possible issues could be contributing to the low signal and broad lines seen and should be examined to improve upon the spectra taken thus far.

Chapter 4

Future Molecules and Ions of Interest

4.1 C_{60} Spectroscopy

After the SCF source is optimized with trioxane, the next step is to move onto a larger molecule. Buckminsterfullerene (C_{60}) has both astronomical and fundamental importance and a high-resolution absorption spectrum of this molecule has not been obtained thus far.

4.1.1 Astronomical Background

C_{60} was first discovered in 1985 by Kroto *et al.* [22] while they were simulating carbon-rich stars in the laboratory. While performing mass spectroscopy of their results they noticed that the number of clusters consisting of 60 carbon atoms dominated over other even numbered clusters. In 2010, the presence of C_{60} was confirmed towards the planetary nebulae Tc1 [23], in addition to reflection nebulae in the interstellar medium (ISM) [24]. These detections were all found through emission spectroscopy of the regions and although it confirmed the presence of extraterrestrial C_{60}, the exact amount present remains a mystery because of uncertainties in the ultraviolet absorption cross-section [24]. Also, these detections required a nearby thermal source or a UV flux large enough to excite the population of C_{60} such that it could emit, which means that the amount of C_{60} in other types of locations is still unknown. By obtaining a high-resolution IR absorption spectrum of C_{60}, observations of the ISM will not have to rely on emission spectroscopy and more information about the number density of C_{60} can be determined. In addition, the low ionization energy of C_{60} makes it a carrier for some of the diffuse interstellar bands (DIBs) from C_{60}^+ absorptions [25, 26].

4.1.2 Spectroscopic Background and Fundamental Interest

A high-resolution rovibrational spectrum of C_{60} is also of great fundamental interest. Since $^{12}C_{60}$ is comprised entirely of bosons, it would be the largest and most symmetric molecule to be observed with rotational resolution. Due to the boson exchange restrictions on the symmetry of the overall wavefunction there are many rotational states which are forbidden [27, 28]. These will appear as "missing" lines in the spectrum,

but at this point no known experimental spectrum has been able to resolve this phenomenon.

Out of the four IR-active bands of C_{60}, one of the F_{1u} vibrational bands is centered near 1185 cm^{-1} [28], which falls within the atmospheric transmission window and the range of our laser system. As such, this band is a prime candidate for study using our system.

4.1.3 Previous Attempts at a High-Resolution Spectrum

Attempts to obtain a high-resolution spectrum of C_{60} have been made previously [29]. Briefly, solid C_{60} was heated to ∼955 K and supersonically expanded through a slit with argon as the carrier gas. C_{60} has negligible vapor pressure at room temperature and the high temperature used in this expansion was needed to get the molecules into the gas phase. Although they had predicted a SNR for the strongest transitions to be ∼130, they were not able to detect anything even by varying a range of the source conditions (temperature, backing pressure, etc.). They came to the conclusion that C_{60} was not sufficiently cooled within the expansion.

The vibrational partition function at a specific temperature, $Q_{vib}(T)$ can be calculated from the sum of all the normal modes, n, where ν_i is the vibrational frequency of the i^{th} normal mode and k_B is the Boltzmann constant [1].

$$Q_{vib}(T) = \prod_{i}^{n} \left(1 - e^{\frac{\nu_i}{k_B T}}\right)^{-1} \tag{4.1}$$

C_{60} has 174 vibrational modes and when the partition function is calculated, Q_{vib} is large even at low temperatures. This affects the ability to observe an absorption spectrum because of the lack of population in the ground state. This can be seen through the Boltzmann distribution [1]:

$$f_0 = \frac{e^{-E_0/(k_B T_{vib})}}{Q_{vib}} \tag{4.2}$$

Although the gas is not likely to exactly follow a Boltzmann distribution, this model provides a good first approximation when considering relative populations. For C_{60}, even at temperatures as low as 190 K, only one molecule in ten is expected to be in the ground state [29].

In addition, the lowest vibrational energy level lies 267 cm^{-1} above the ground state. This is much higher than other polyaromatic hydrocarbons (PAHs) which have previously been studied in a supersonic expansion with a lowest excited state around 30 - 100 cm^{-1}. This means that the vibrational to translational energy transfer between C_{60} and the carrier gas has to be very efficient since this transfer becomes more difficult with the increasing energy gap [29].

For these reasons, a SCF expansion would be beneficial in providing a lower starting temperature for

C_{60}. With a 7:3 mole fraction ratio of CO_2:toluene and a critical temperature of 445 K, Q_{vib} for C_{60} will be $\sim$1.8 x 10^8, which is significantly lower than 1.3 x 10^{28} at 955 K.

4.1.4 High Repetition Rate Ringdown

The current instrumental system is able to achieve sensitivities on the order of $\sim 10^{-9}$ cm^{-1} Hz$^{-1/2}$ [6]; however, increasing the sensitivity will increase the expected SNR for C_{60} and any other molecules observed in the future. The most efficient way to accomplish this would be by locking the laser to the cavity in order to increase the ringdown rate.

One technique that could be used is Pound-Drever-Hall (PDH) locking [30]. PDH locking uses the backreflected light from the cavity mirrors and relies on the effects of absorption and dispersion of light. When the laser matches up to the cavity FSR, the cavity acts as an absorber and the dispersion signal is monitored. Since this signal has a zero crossing at the absorption wavelength, any deviation from zero sends fast corrections back to the laser. In this way, light is able to continuously build up in the cavity.

By locking to the cavity instead of dithering the cavity length, the number of ringdown events will increase from 100 Hz to greater than 10 kHz. Since sensitivity is inversely proportional to the square root of the ringdown rate, this will increase the sensitivity to $\sim 10^{-10}$ cm^{-1} Hz$^{-1/2}$ [31]. This factor of ten improvement will be extremely useful when searching for C_{60} lines within the SCF expansion, since the mass flow rate is expected to be on the order of a few milligrams per hour instead of the 0.7 - 2.0 g/hr seen with the oven-heated source [32].

4.2 CH_5^+ Spectroscopy

Another direction to take the system is towards ion spectroscopy. CH_5^+ is a fundamentally interesting ion and also has a bending mode which lies within the current frequency range of the QCL.

4.2.1 Spectroscopic Background and Fundamental Interest

The highly fluxional molecular ion CH_5^+ was first observed in 1999 by White *et al.* between 2770 - 3150 cm^{-1} [33]. In this region they observed $\sim$900 lines, most of which remain unassigned to this day. The potential energy surface consists of 120 equivalent minima from C_s symmetry, and the saddle points on this surface correspond to a rotational motion of a hydrogen pair at $\sim$40 cm^{-1}, as well as a flipping motion of the protons which occurs $\sim$300 cm^{-1} [34,35]. Overall, the classical description of CH_5^+ assumes the protons are continuously scrambling around the central carbon atom. It is due to this high fluxionality that the

assignment of the transitions observed over 15 years ago still remain a mystery, although recent attempts have moved closer to assignment through combination differences [36].

4.2.2 Bending Mode

A low-resolution spectrum of CH_5^+ has been observed using a laser induced reaction (LIR) spectroscopy method [37]. From this experiment, three main bands were seen and assigned to different motion types of the molecule [35]. One of these bands is a bending-type band centered ∼1250 cm^{-1}, which is within the frequency range of the current QCL chip. From the LIR experiment, it is found that the intensity of this band is ∼30% of that of the stretching band located at ∼3000 cm^{-1} which was observed previously. The most intense transition observed from the stretching band had a SNR ∼20 with an experimental pathlength of 8 m and a noise-equivalent absorption (NEA) of ∼4 x 10^{-6}.

To observe the bending mode transition with CRDS the estimated SNR would be ∼600 for the strongest transitions. This estimation comes from an expected decrease in intensity of ∼70% when comparing the two bands, and an effective pathlength of ∼2 km for a positive column cavity (1 m in length) with the current mirrors and approximate NEA of the current system of 1 ppm [6].

4.2.3 Positive Column Cavity Ringdown Spectroscopy

CH_5^+ has already been observed in a positive column source by Hodges *et al.* in 2013 [38]. The spectroscopy done was using a technique called Noise-Immune Cavity-Enhanced Optical Heterodyne Velocity Modulation Spectroscopy (NICE-OVHMS) at ∼2898.008 cm^{-1}.

For future spectroscopy of CH_5^+ and other ions around 8.5 μm, the EC-QCL light source and SOF locking system will remain the same but the sample introduction will move from a supersonic expansion for neutral molecules to a positive column for the production of ions. The source cell itself is ∼1 meter in length and consists of a triple jacket design around the column to allow for liquid nitrogen cooling. The main projected challenge in setting up this source is maintaining the finesse of the cavity in order to allow for CRDS while ensuring the plasma does not interact with a piezo-electric transducer on the mirrors.

The finesse of the current cavity is ∼6000, which gives an effective pathlength of 2 km for a 1 m cavity, which would be the approximate length of an ion cell. This large pathlength is an advantage of CRDS which allows for the detection of absorption features on the order of parts-per-million. One issue that could pose a problem for this setup is that the most common method used to isolate the plasma from the cavity mirrors is to use windows on the ends of the cell which are cut at Brewsters angle. Theoretically windows set at Brewsters angle should allow for perfect transmission through the glass, but slight uncertainties in the

position, in addition to scanning through a frequency range, makes losses through these windows significant. Although it is technically possible to do CRDS with Brewster windows, it may not be the most ideal solution.

Another option would be to confine the plasma to the central region away from the mirrors using magnets. The average drift velocity, v, of electrons within a plasma is on the order of $\sim 10^6$ m/s [39]. To estimate the magnetic strength, B, needed to divert the electrons, the radius of curvature, r, can be calculated using the mass of the electrons, m, and the charge, q via the formula presented below.

$$B = \frac{mv_{\perp}}{qr} \tag{4.3}$$

The resulting magnetic strength needed from this estimation is $\sim$6 G, a value that should be easily obtainable using commercial magnets. Since the plasma is quasi-neutral, confining the electrons should also encourage confinement of the ions present. Preliminary testing found that this technique directs the plasma along the magnetic field lines but does not encourage enough recombination to prevent the plasma from discharging to the mirrors. Machining some of the current metallic parts out of a dielectric material could further reduce discharges and encourage the plasma to travel between the two electrodes instead of the mirrors.

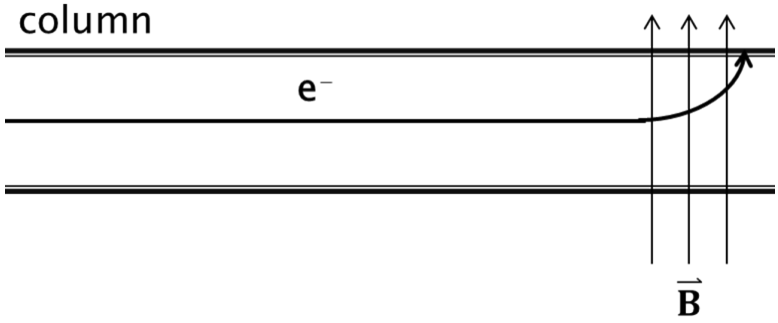

Figure 4.1: Electron movement with a magnetic field. The theoretical electron movement with an applied external field is shown. The electrons are deflected such that they collide with the column walls.

Chapter 5

Temperature Determination from C_3 Observations

In addition to the laboratory work presented above, we have also undertaken theoretical work on a related species, C_3. Although the transitions studied for C_3 are combination rotational-vibrational-electronic (rovibronic) transitions that do not appear in our spectroscopic wavelength, we have done modeling of the temperature dependence of the molecule to fit with astrochemical observations. Details of this work follows.

5.1 Astronomical Significance

The polyatomic molecule C_3 is an important molecule in the interstellar medium (ISM) for a variety of reasons. It is related to longer carbon chains, which are thought to be a possible source of the DIBs [40], which remain unassigned to this day. In addition, the temperature and column density of interstellar clouds can be determined and then compared to data from C_2 observations along the same sightlines. From previous observations it is thought that C_2 and C_3 are related through the same chemical pathway in the ISM [41]. C_2 has already been used as a probe for temperature and density in these clouds, and the same concept should be able to be applied to C_3. By then comparing the results to what is already known from C_2 [42–44] more information can be determined about the environment in the ISM.

5.2 Observational and Modeling Background

In 1881, spectral lines around 4050 Å were observed by Huggins *et al.* [45] while observing a comet. These were eventually attributed to C_3 in 1951 [46]. The first interstellar observation of C_3 came in 1988 when the anti-symmetric stretch of C_3 around 2050 cm^{-1} was detected towards IRC+10216 [47]. Then, in 2000, the bending mode, which occurs around 63 cm^{-1}, was detected towards both Sgr B2 and IRC+10216 [48]. It wasn't until a year later, in 2001, that the rovibronic transition at 4050 Å was observed in the interstellar medium towards ζ Oph, ζ Per, and 20 Aql [49].

The column density of C_3, kinetic temperature, and collisional number density towards sightlines in the ISM have been determined previously using a variety of techniques. Briefly, these parameters were

determined from the rovibronic transitions observed in 2001, in addition to another observation along HD 210121 [50]. In this case, the column density was determined from the equivalent widths of the lines, and the temperature and collisional number density were calculated using models to fit the spectra. Several years later the same rovibrational transition of C_3 around 4050 Å was observed towards ten additional sightlines [44]. This time, a fitting procedure was used in order to determine the column density, and temperature was estimated from a Boltzmann analysis of the results. Most recently, observational data was collected again along HD 169454 [51]. The column density distribution of this observation was calculated from equivalent widths, and the temperature and collisional number density were determined through modeling. The unique aspect of this analysis was that Schmidt *et al.* took into account contributions from perturber lines which occur from intensity borrowing from the excited $A^1\Pi_u$ state to nearby states. They calculated the frequency and oscillator strengths of these lines from high-resolution laboratory spectra. However, none of these previous calculations used fitting procedures and models for both the column density, and the temperature and collisional number density determinations.

5.3 Spectroscopic Information

C_3 is a homonuclear linear triatomic molecule without a permanent dipole moment. Since it does not have a permanent dipole moment it lacks allowed rotational transitions, which make the rovibronic transitions between $A^1\Pi_u \leftarrow X^1\Sigma_g^+$ of significant interest. Because of symmetry constraints only even J-levels, which are symmetric, exist in the ground state, $X^1\Sigma_g^+$, resulting in some "missing" lines in the resulting spectrum [52].

5.4 Determining Column Density

The column density towards the ten sightlines from 2003 were calculated using a fitting algorithm similar to the one used previously in those simulations [44]. Briefly, the fitting program varies the populations of the different rotational levels until all P, Q, and R transition lines are optimized to the observational data. Since perturber line oscillator strengths and frequencies are now available, these transitions were also included in the fitting [51].

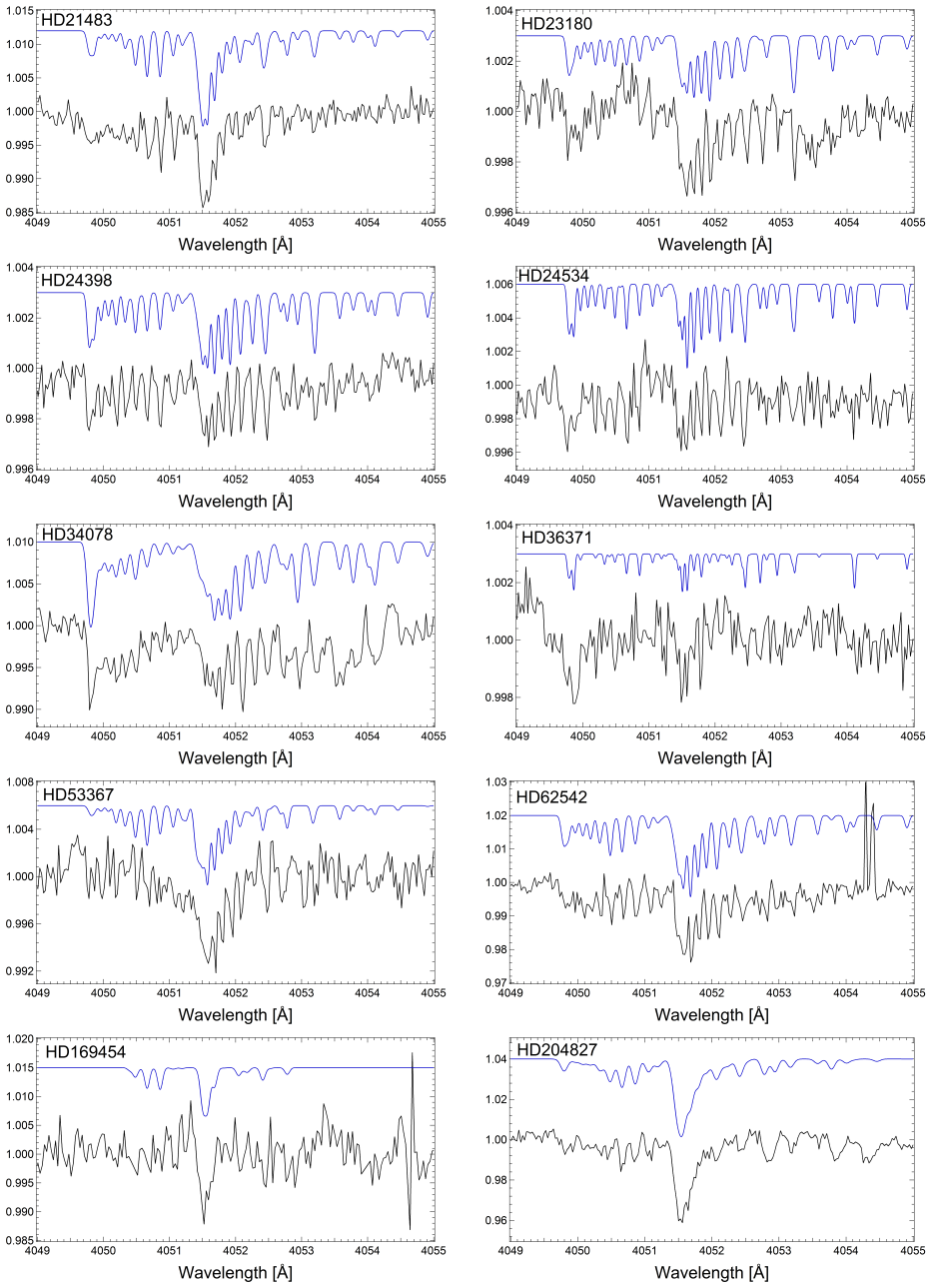

Figure 5.1: C_3 column density modeling. The ten sightlines were fit with a model that adjusts the rotational populations in order to best fit the P, Q, and R lines associated with each rotational level. The top traces (blue) are the model fit and the bottom traces (black) are what was observed previously [44].

Table 5.1: Rotational column density towards different sightlines. The C_3 column density towards the ten sightlines for each of the ground state rotational levels obtained by the fitting procedure described.

	N_J (x10^{11} cm^{-2})									
J	HD 2148 3	HD23180	HD 24398	HD 24534	HD 34078	HD 36371	HD 53367	HD 62542	HD 169454	HD 204827
0	1.06	0.00	0.24	0.16	0.54	0.05	1.46	1.06	0.00	1.13
2	5.43	0.78	0.97	1.28	2.65	0.25	2.65	5.55	0.45	14.16
4	8.48	1.16	1.65	1.55	2.43	0.52	2.97	10.51	5.53	23.55
6	8.90	1.41	1.81	2.32	4.98	0.50	4.39	14.22	5.51	27.88
8	7.10	1.56	2.01	1.87	7.91	0.23	3.72	16.61	2.65	22.76
10	3.79	1.43	1.57	1.44	7.18	0.30	2.53	12.09	0.00	11.73
12	2.37	1.66	1.79	1.34	8.10	0.12	2.22	10.81	0.00	6.58
14	1.95	0.95	1.33	1.46	6.86	0.00	0.76	9.53	0.00	5.88
16	1.38	1.07	1.27	1.34	4.91	0.15	0.59	6.51	0.00	2.75
18	2.07	0.73	0.47	1.52	3.32	0.44	0.11	5.47	0.00	0.08
20	1.12	0.12	0.79	0.67	2.19	0.39	0.47	4.44	0.00	0.00
22	0.90	0.00	1.24	0.55	6.41	0.29	0.00	4.20	0.00	6.66
24	1.86	1.20	1.24	1.08	2.58	0.24	0.20	2.95	0.00	0.15
26	0.00	0.00	0.00	0.32	0.00	0.00	0.00	0.00	0.00	0.00
28	1.17	1.20	0.43	0.93	4.31	0.00	0.31	0.87	0.00	5.26
30	1.59	0.23	0.57	1.06	4.47	0.46	0.52	2.36	0.00	0.45
δN_J^{a*}	0.40	0.21	0.17	0.27	0.38	0.15	0.31	0.57	0.96	0.76

[a] The 1σ uncertainty for δN_J is based off calculations using the oscillator strength. Detailed explanations and calculations can be found in Ádámkovics *et al.* [44]

[*] δN_J for R(0) is half the listed value.

5.5 Non-LTE Modeling

As seen from the resulting column density distributions, the molecules towards these sightlines do not conform to a strictly Boltzmann distribution, which would be expected if the system was under local thermodynamic equilibrium (LTE). However, since they seem to be in non-LTE environments, the fitting model to determine temperature and collisional number density needs to take into account different formation and destruction terms for each rotational level. This was accomplished using a program called RADEX [53] and adjusting the inputs as needed. Overall, the model assumes that the system is in a steady state [54], so that the change in population for each level, n_x, does not change over time, t.

$$\frac{dn_x}{dt} = 0 \tag{5.1}$$

In effect, none of the populations for the levels will be changing over time, so the rate of molecules leaving each state are equal to the rate of molecules entering each state.

5.5.1 Radiative Transitions

The different radiative transitions for a molecule include absorption, and spontaneous and stimulated emission. Based on previous works, three excited states and the ground state were included in the calculations for C_3 [50]. These were the A(000) state, which is the transition of interest, the X(001) state, and the X(010) state. Transitions from the ground to the X(001) state occur around 2050 cm^{-1} and correspond to an anti-symmetric stretching mode of the molecule. The X(010) band is a bending mode and occurs around 63 cm^{-1}. Before the radiative transitions could be calculated, the rotational energy levels of the ground state and each excited state were calculated based on known molecular constants.

The energy levels for the ground state X(000) were calculated using the equation below with molecular constants from Tanabashi *et al.* [55]. Since it is the lowest state, the energy of v_0 is zero and is not included in the expression.

$$E = BJ(J+1) - DJ^2(J+1)^2 + HJ^3(J+1)^3 \tag{5.2}$$

The energy levels for the bending mode X(010) were calculated with a similar expression, with a few extra terms added to account for ℓ-type doubling. The expression and molecular constants for X(010) came from the work of Gendriesch *et al.* [56]

$$E = v_0 + B[J(J+1) - \ell^2] - D[J(J+1) - \ell^2]^2 + H[J(J+1) - \ell^2]^3 \pm \frac{1}{2}[q_\ell J(J+1) + q_D J^2(J+1)^2 + q_H J^3(J+1)^3] \tag{5.3}$$

The bending mode has Π_u symmetry and since the selection rule for electronic transitions between Σ and Π electronic states is $+ \leftrightarrow -$, no splitting is observed between the transitions even with ℓ-type doubling. Instead, the R and P transitions occur from the lower of the ℓ-doubled levels and the Q transitions occur from the higher of the ℓ-doubled levels.

The energy levels for the anti-symmetric stretch X(001) were calculated using the same equation that was used for the ground state, but with v_o and an additional centrifugal distortion term, $MJ^5(J+1)^5$, included. Molecular constants for this state were from Matsumura *et al.* [57]

For the A(000) energy state, the levels were again calculated using molecular constants from Tanabashi *et al.* [55] and the following equation in order to account for ℓ-type doubling.

$$E = v_0 + BJ(J+1) - D[J(J+1)]^2 + H[J(J+1)]^3 \pm \frac{1}{2}qJ(J+1) \tag{5.4}$$

For the transition between A(000) ← X(000), no splitting will be seen because of the symmetry considerations already explained for the X(010) ← X(000) transition.

The Einstein coefficient A, which describes spontaneous emission, was then calculated for each transition. For the X(000) ← X(001) and X(000) ← X(010) transitions, A was calculated with the following equation based on values of the transition dipole moment, μ, of 0.19 Debye and 0.44 Debye for X(000) and X(001) respectively [58].

$$A = \frac{64\pi^4}{3c^3h}\nu^3|\mu_{12}|^2 \tag{5.5}$$

The Einstein coefficient A for the X(000) ← A(000) transition was calculated using a slightly different variation of the expression which relies on the electronic oscillator strength, f, and the statistical weights of the rotational levels, g_1 and g_2.

$$A = \frac{8\nu^2\pi^2e^2}{mc^3}\frac{g_1}{g_2}f \tag{5.6}$$

For the rovibronic transitions, oscillator strengths for each transition was taken from Schmidt *et al.* [51] when possible because of the new perturber data included and Ádámkovics *et al.* [44] for any that were not available with the new perturbed transitions.

Quadrupole transitions within the ground state were also included using the quadropole moment, Q, of 2.26 AU for C_2 [43, 50], since the value for C_3 is unknown.

$$A = \frac{32\pi^6}{5h}\nu^5Q^2\frac{(J''+1)(J''+2)}{(2J'+1)(2J''+3)} \tag{5.7}$$

With the Einstein A coefficients calculated for each transition, the Einstein B coefficients, which describe absorption and stimulated emission for each transition, were calculated using the Einstein relations and the principle of detailed balance within the RADEX program [54].

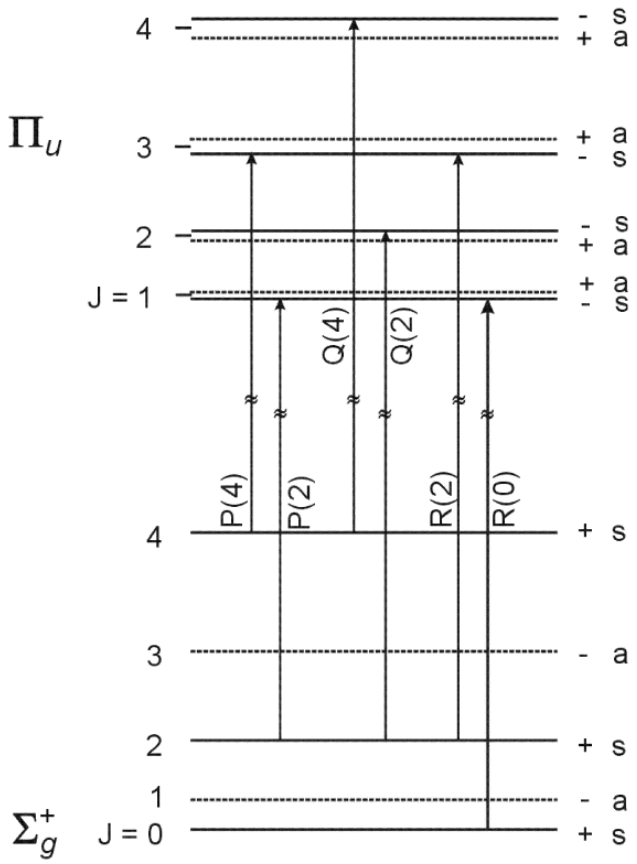

Figure 5.2: C_3 transitions between X(010) ← X(000). The different parities of the rotational levels are shown for the Σ_g^+ and Π_u energy levels. Only allowed transitions occur, which result in no splitting from ℓ-type doubling. Figure adapted from Gendriesch *et al.* [56].

5.5.2 Collisional Rates

Collisions also play a part in the transitions between different energy levels. For C_3, collisional rate coefficients between C_3 and He have recently been calculated for the ground state rotational levels up to J=10, with a ΔJ of 2 and 4 [59]. In order to account for the difference between He and H_2, these rates were scaled by 1.38 [51]. Additional collisional excitation values were extrapolated based on the exponential-energy gap law behavior [59] such that rates were estimated for all ΔJ's up to the highest rotational level of J=50. De-excitation rates are again calculated using the principle of detailed balance within the RADEX program [54].

5.6 Initial Results

All ten sightlines from 2003 [44] were modeled with RADEX [53] at a variety of different temperatures and collisional densities, and the best fit was chosen using goodness-of-fit criteria. None of the results obtained were collisionally dependent. For sightlines HD 21483, HD 53367, and HD 204827, the predicted values were reasonably close to the previous low temperature estimations from Boltzmann analyses. In addition, all of the sightlines, except HD 36371, that previously had a low and high temperature regime were fit to a value that was in-between the previous values. By plotting the column densities against the model's prediction, it was seen that the lower rotational levels usually fit reasonably well, but that the model deviates at the higher levels.

Table 5.2: Temperature and collisional modeling of C_3. The results from the first attempt RADEX [53] models are shown below. Although a couple of the sightlines seem to be close to previously predicted values, many seem to have large deviations from the previous values.

Sightline	Best Fit Kinetic Temperature (K)		
	Current Fit	Previous Boltzmann Analysis (T_{low},T_{high}) [44]	Previous C_2 Temperature [44]
HD 21483	45	40, 560	13 ± 5
HD 23180	125	90, 470	60 ± 20
HD 24398	140	90, 235	80 ± 15
HD 24534	160	81, 408	44 ± 5
HD 34078	190	171, 275	120 ± 10
HD 36371	undetermined	38 ,554	...
HD 53367	50	40, 366	...
HD 62542	100	75, 137	36 ± 15
HD 169454	35	42	> 500
HD 204827	45	43	630 ± 200

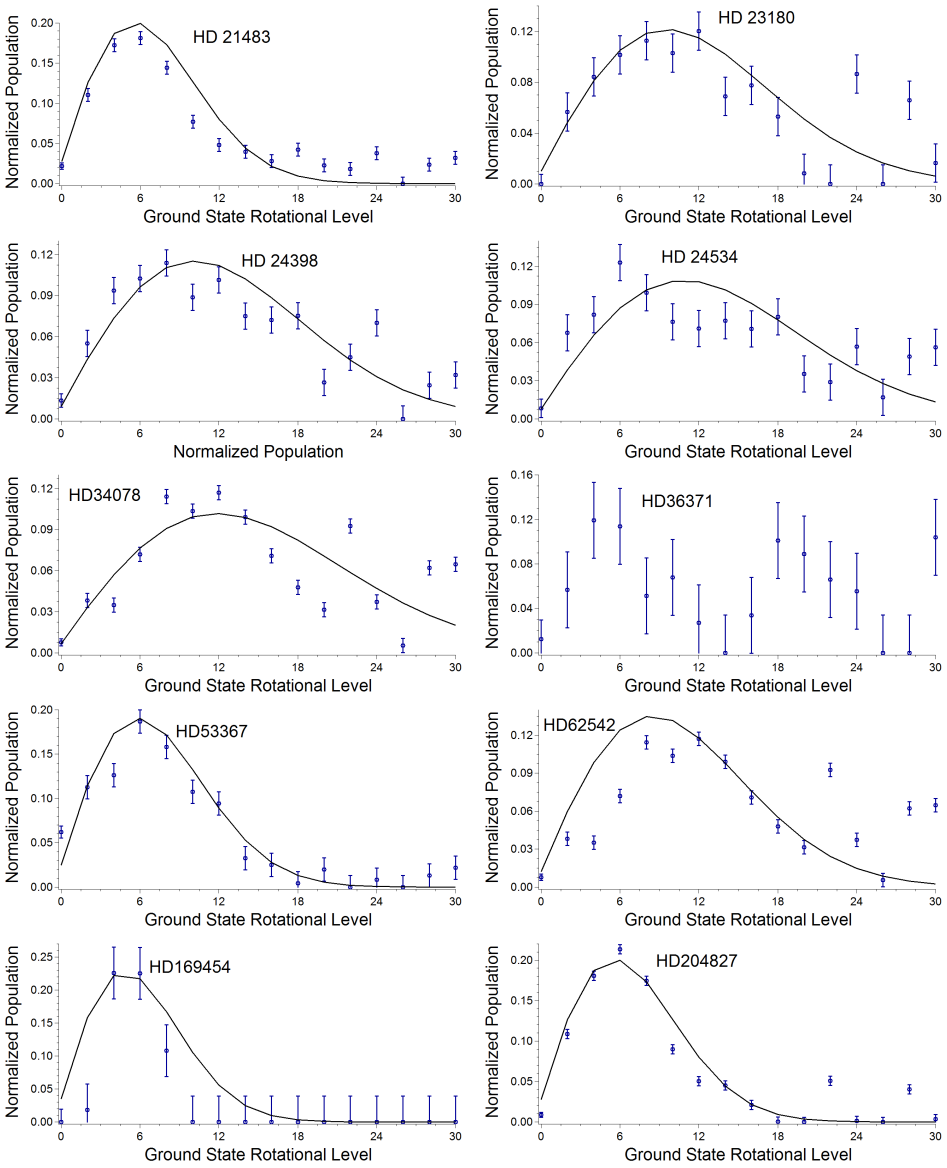

Figure 5.3: C_3 column density comparison. The normalized rotational populations for each sightline were compared to the modeled values (shown in blue). Many of the fits seem to describe the lower rotational levels relatively well, but highly deviate with the higher rotational levels.

5.7 Destruction Terms

Although RADEX [53] is programmed for non-LTE modeling, it seemed to have difficulty properly fitting the data provided for C_3. This result can be attributed to an omission in the program of formation pumping of C_3, which would affect the populations of the higher rotational levels. In the past, other models have

found success in using a destruction rate on the order of $\sim 10^{-9}$ s^{-1} [50, 51], in which the molecule is then re-introduced into the system with a Boltzmann rotational distribution at a specified formation temperature. Including this term in the model should allow it to better fit the data.

Once the temperature and collisional number densities are determined for C_3, this data can then be compared to data already available from C_2. By comparing the two, more information about the relationship between C_2 and C_3 in the ISM and the conditions of these clouds can be determined.

Chapter 6

Conclusions

We have shown preliminary results for laboratory rovibrational and theoretical rovibronic spectroscopic studies of carbon-containing molecules. Additional work is needed to improve the sensitivity of the EC-QCL CRDS instrument and reliability of the SCF expansion source to make further observations of 1,3,5-trioxane. Other astrochemically important species with transitions in the far mid-IR were also discussed and adjustments to the current system were proposed in order to better observe these molecules and ions. These possible future studies present a wide range of interesting features, including observing the "missing" transitions of C_{60} and obtaining a high-resolution spectrum of the bending mode of the highly fluxional ion CH_5^+. With the theoretical work, the initial rovibronic modeling of C_3 shows the temperature dependence of this molecule in the ISM. The destruction term is proposed as an additional variable to be considered in the model, which would allow collisional data to be incorporated in the results.

References

[1] Peter F. Bernath. *Spectra of Atoms and Molecules*. Oxford University Press, 2nd edition, 2005.

[2] G.Wysocki, R.F. Curl, F.K. Tittel, R. Maulini, J.M. Bulliard, and J. Faist. Widely tunable mode-hop free external cavity quantum cascade laser for high resolution spectroscopic applications. *Applied Physics B*, 81:769–777, 2005.

[3] The HITRAN Database. `https://www.cfa.harvard.edu/hitran/`.

[4] Bradley M. Gibson, Nicole C. Koeppen, and Benjamin J. McCall. Rotationally-resolved spectroscopy of the ν_{16} band of 1,3,5-trioxane. *Journal of Molecular Spectroscopy*, 317:47–49, 2015.

[5] Bradley M. Gibson and Benjamin J. McCall. Tilt-tuned etalon locking for tunable laser stabilization. *Optics Letters*, 2015:2696–2698, 2015.

[6] Brian Brumfield. *Development of a quantum cascade laser based spectrometer for high-resolution spectroscopy of gas phase C_{60}*. PhD thesis, University of Illinois, 2011.

[7] Gianluca Gagliardi. *Cavity-Enhanced Spectroscopy and Sensing*. Springer, 2014.

[8] Chung Hang Sin, Matthew R. Linford, and Steven R. Goates. Supercritical fluid/supersonic jet spectroscopy with a sheath-flow nozzle. *Analytical Chemistry*, 64:233–238, 1992.

[9] Hervé Cottin, Marie-Claire Gazeau, Jean-François Doussin, and François Raulin. An experimental study of the photodegradation of polyoxymethylene at 122, 147, and 193 nm. *Journal of Phochemistry and Photobiology A: Chemistry*, 135(1):53–64, 2000.

[10] Hervé Cottin, Yves Bénilan, Marie-Claire Gazeau, and François Raulin. Origin of cometary extended sources from degradation of refractory organics on grains: polyoxymethylene as formaldehyde parent molecule. *Icarus*, 167(2):397–416, 2004.

[11] Takeshi Oka, Katsura Tsuchiya, Suehiro Iwata, and Yonezo Morino. Microwave spectrum of s-trioxane. *Bulletin of the Chemical Society of Japan*, 37:4–7, 1964.

[12] Jean Bellet, Jean-Marcel Colmont, and Jean Lemaire. Millimeter wave study of the ground state and several excited vibrational states of trioxane. *Journal of Molecular Spectroscopy*, 34(2):190–205, 1970.

[13] J.M. Colmont. Microwave spectrum of trioxane in four excited degenerate vibrational states, especially in the $2\nu_{20}$(E) state and the combination state $\nu(A_1) + \nu_{20}$(E). *Journal of Molecular Spectroscopy*, 58(2):220–228, 1975.

[14] Jean-Marcel Colmont. Assignment of the microwave spectrum of trioxane in the $\nu_{19}(E) = \nu_{20}(\mathrm{E}) = 1$ state. *Journal of Molecular Structure*, 62:85–94, 1980.

[15] Jean-Marcel Colmont. Assignment method of the rotational spectrum of a slightly asymmetric molecule: application to the ^{13}C and ^{18}O species of the molecule of trioxane. *Journal of Molecular Spectroscopy*, 80(1):166–177, 1980.

[16] J. Gadhi, G. Wlodarczak, D. Boucher, and J. Demaison. The submillimeter-wave spectrum of trioxane. *Journal of Molecular Spectroscopy*, 133(2):406–412, 1989.

[17] J-F. Henninot, H. Bolvin, J. Demaison, and B. Lemoine. The infrared spectrum of trioxane in a supersonic slit jet. *Journal of Molecular Spectroscopy*, 152(1):62–68, 1992.

[18] C. Western. Pgopher, a program for simulating rotational structure, 2009. University of Bristol.

[19] Kiyokatsu Jinno and Chikayuki Kohrikawa. Supercritical and subcritical fluid extraction of fullerenes from carbon soot. *Chimica Oggi*, 16:9–15, 1998.

[20] S. Saim, K.C. Kuo, and D.L. Stalling. Supercritical fluid extraction of fullerenes C_{60} and C_{70} from carbon soot. *Separation Science and Technology*, 28(8):1509–1525, 1993.

[21] Steven R. Goates, Norman A. Zabriskie, John K. Simons, and Bahram Khoobehi. Detection of aerosol formation in the effluent of a supercritical fluid chromatograph. *Analytical Chemistry*, 59:2927–2930, 1987.

[22] H.W. Kroto, J.R. Heath, S.C. O'Brien, R.F. Curl, and R.E. Smalley. C_{60}: Buckminsterfullerene. *Nature*, 318:162–163, 1985.

[23] Jan Cami, Jeronimo Bernard-Salas, Els Peeters, and Sarah Elizabeth Malek. Detection of C_{60} and C_{70} in a young planetary nebula. *Science*, 329:1180–1182, 2010.

[24] Kris Sellgren, Michael W. Werner, James G. Ingalls, J.D.T. Smith, T.M. Carleton, and Christine Joblin. C_{60} in reflection nebulae. *The Astrophysical Journal Letters*, 722(1):L54–L57, 2010.

[25] G.H. Herbig. The diffuse interstellar bands. *Astronomy & Astrophysics*, 33:19–73, 1995.

[26] E.K. Campbell, M. Holz, D. Gerlich, and J.P Maier. Laboratory confirmation of C_{60}^+ as the carrier of two diffuse interstellar bands. *Nature*, 523:322–323, 2015.

[27] R. Saito, G. Dresselhaus, and M.S. Dresselhaus. Hindered rotation of solid $^{12}C_{60}$ and $^{13}C_{60}$. *Physical Review B*, 50(8):5680–5688, 1994.

[28] Norihito Sogoshi, Yoshiyasu Kato, Tomonari Wakabayashi, Takamasa Momose, Simon Tam, Michelle E. DeRose, and Mario E. Fajardo. High-resolution infrared absorption spectroscopy of C_{60} molecules and clusters in parahydrogen solids. *The Journal of Physical Chemistry A*, 104(16):3733–3742, 2000.

[29] Jacob T. Stewart, Brian E. Brumfield, Bradley M. Gibson, and Bengamin J. McCall. Inefficient vibrational cooling of C_{60} in a supersonic expansion. *ISRN Physical Chemistry*, 2013, 2013.

[30] R.W.P. Drever, J.L. Hall, F.V. Kowalski, J. Hough, G.M. Ford, A.J. Munley, and H. Ward. Laser phase and frequency stabilization using an optical resonator. *Applied Physics B*, 31:97–105, 1983.

[31] R.Z. Martínez, Markus Metsälä, Olavi Vaittinen, Tommi Lantta, and Lauri Halonen. Laser-locked, high-repetition-rate cavity ringdown spectrometer. *Journal of the Optical Society of America B*, 23(4):727–740, 2006.

[32] Bradley Michael Gibson. *High-resolution infrared spectroscopy in pursuit of C_{60} and other astrochemical targets*. PhD thesis, University of Illinois, 2015.

[33] Edmund T. White, Jian Tang, and Takeshi Oka. CH_5^+: The infrared spectrum observed. *Science*, 284:135–137, 1999.

[34] Xiao-Gang Wang and Tucker Carrington Jr. Vibrational energy levels of CH_5^+. *The Journal of Chemical Physics*, 129:234102, 2008.

[35] Xinchuan Huang, Anne B. McCoy, Joel M. Bowman, Lindsay M. Johnson, Chandra Savage, Feng Dong, and David J. Nesbitt. Quantum deconstruction of the infrared spectrum of CH_5^+. *Science*, 311:60–63, 2006.

[36] Oskar Asvany, Koichi M.T. Yamada, Sandra Brünken, Alexey Potapov, and Stephan Schlemmer. Experimental ground-state combination difference of CH_5^+. *Science*, 347:1346–1349, 2015.

[37] Oskar Asvany, Padma Kumar P, Britta Redlich, Ilka Hegemann, Stephan Schlemmer, and Dominik Marx. Understanding the infrared spectrum of bare CH_5^+. *Science*, 309:1219–1222, 2005.

[38] James N. Hodges, Adam J. Perry, Paul A. Jenkins, Brian M. Siller, and Benjamin J. McCall. High-precision and high-accuracy rovibrational spectrosocpy of molecular ions. *The Journal of Chemical Physics*, 139:164201, 2013.

[39] A. von Engel. *Ionized Gases*. American Institute of Physics, 2nd edition, 1994.

[40] A.E. Douglas. Origin of diffuse interstellar lines. *Nature*, 269:130–132, 1977.

[41] Takeshi Oka, Julie A. Thorburn, Bengamin J. McCall, Scott D. Fridman, Lewis M. Hobbs, Paule Sonnentrucker, Daniel E. Welty, and Donald G. York. Observations of C_3 in translucent sight lines. *The Astrophysical Journal*, 582:823–829, 2003.

[42] Silvia Casu and Cesare Cecchi-Pestellini. Excitation of C_2 in diffuse interstellar clouds. *The Astrophysical Journal*, 749(1):48, 2012.

[43] Ewine F. van Dishoeck and John H. Black. The excitation of interstellar C_2. *The Astrophysical Journal*, 258:533–547, 1982.

[44] Máté Ádámkovics, Geoffrey A. Blake, and Benjamin J. McCall. Observations of rotationally resolved C_3 in translucent sight lines. *The Astrophysical Journal*, 595:235–246, 2003.

[45] William Huggins. Preliminary note on the photographic spectrum of Comet b 1881. *Proceedings of the Royal Society of London*, 33:1–3, 1881.

[46] A.E. Douglas. Laboratory studies of the λ4050 group of cometary spectra. *Astrophysical Journal*, 114:466–468, 1951.

[47] Kenneth W. Hinkle, John J. Keady, and Peter F. Bernath. Detection of C_3 in the circumstellar shell of IRC+10216. *Science*, 241(4871):1319–1322, 1988.

[48] José Cernicharo and Javier R. Goicoechea. Far-infrared detection of C_3 in Sagittartius B2 and IRC +10216. *The Astrophysical Journal*, 534:L199–L202, 2000.

[49] John P. Maier, Nicholas M. Lakin, Gordon A.H. Walker, and David A. Bohlender. Detection of C_3 in diffuse interstellar clouds. *The Astrophysical Journal*, 553(1):267–273, 2001.

[50] E. Roueff, P. Felenbok, J.H. Black, and C. Gry. Interstellar C_3 toward HD 210121. *Astronomy & Astrophysics*, 384:629–637, 2002.

[51] M.R. Schmidt, J. Krelowski, G.A. Galazutdinov, D. Zhao, M.A. Haddad, W. Ubachs, and H. Linnartz. Detection of vibronic bands of C_3 in a translucent cloud towards HD 169454. *Monthly Notices of the Royal Astronomical Society*, 441:1134–1146, 2014.

[52] Gerhard Herzberg. *Molecular Spectra and Molecular Structure*. D. Van Nostrand Company, 2nd edition, 1950.

[53] F.F.S. van der Tak, J.H. Black, F.L. Schöier, D.J. Jansen, and E.F. van Dishoeck. RADEX, a computer program for performing statistical equilibrium calculations,2007. `http://home.strw.leidenuniv.nl/~moldata/radex.html`.

[54] F.F.S. van der Tak, J.H. Black, F.L. Schöier, D.J. Jansen, and E.F. van Dishoeck. A computer program for fast non-LTE analysis of interstellar line spectra. *Astronomy & Astrophysics*, 468:627–635, 2007.

[55] A. Tanabashi, T. Hirao, T. Amano, and P.F. Bernath. Fourier transform emission spectra of the (000)-(000) band of the λ4051.6 band of C_3. *The Astrophysical Journal*, 624:1116–1120, 2005.

[56] Ralf Gendriesch, Kai Pehl, Thomas Giesen, Gisbert Winnewisser, and Frank Lewen. Terahertz spectroscopy of linear triatomic CCC: High precision laboratory measurement and analysis of the rovibrational bending transitions. *Zeitschrift für Naturforschung*, 58a:129–138, 2003.

[57] Keiji Matsumura, Hideto Kanamori, Kentarou Kawaguchi, and Eizi Hirota. Infrared diode laser kinetic spectroscopy of the ν_3 band of C_3. *The Journal of Chemical Physics*, 89(6), 1988.

[58] C.A. Schmuttenmaer, R.C. Cohen, N. Pugliano, J.R. Heath, A.L. Cooksy, K.L. Busarow, and R.J. Saykally. Tunable far-IR laser spectroscopy of jet-cooled carbon clusters: the nu 2 bending vibration of C_3. *Science*, 249(4971):897–900, 1990.

[59] Daniel G.A. Smith, Konrad Patkowski, Duy Trinh, N. Balakrishnan, Teck-Ghee Lee, Robert C. Forrey, B.H. Yang, and P.C. Stancil. Highly correlated electronic structure calculations of the He-C_3 van der Waals complex and collision-induced rotational transitions of C_3. *The Journal of Physical Chemistry A*, 118:6351–6360, 2014.